Measurement of optical second-harmonic generation from an individual single-walled carbon nanotube

2013 New J. Phys. 15 083043

(http://iopscience.iop.org/1367-2630/15/8/083043)

New Journal of Physics
The open access journal for physics

Measurement of optical second-harmonic generation from an individual single-walled carbon nanotube

M J Huttunen[1], O Herranen[2], A Johansson[2,5], H Jiang[3], P R Mudimela[3], P Myllyperkiö[4], G Bautista[1], A G Nasibulin[3], E I Kauppinen[3], M Ahlskog[2], M Kauranen[1] and M Pettersson[4]

[1] Department of Physics, Tampere University of Technology, PO Box 692, FI-33101 Tampere, Finland
[2] Nanoscience Center, Department of Physics, University of Jyväskylä, PO Box 35, FI-40014 Jyväskylä, Finland
[3] Department of Applied Physics and Center for New Materials, Aalto University, Puumiehenkuja 2, FI-00076 Aalto, Finland
[4] Nanoscience Center, Department of Chemistry, University of Jyväskylä, PO Box 35, FI-40014 Jyväskylä, Finland
E-mail: andreas.johansson@jyu.fi

New Journal of Physics **15** (2013) 083043 (14pp)
Received 7 May 2013
Published 22 August 2013
Online at http://www.njp.org/
doi:10.1088/1367-2630/15/8/083043

Abstract. We show that optical second-harmonic generation (SHG) can be observed from individual single-walled carbon nanotubes (SWCNTs) and, furthermore, allows imaging of individual tubes. Detailed analysis of our results suggests that the structural non-centrosymmetry, as required for SHG, arises from the non-zero chiral angle of the SWCNT. SHG thus has potential as a fast, non-destructive and simple method for imaging of individual nanomolecules and for probing their chiral properties.

[5] Author to whom any correspondence should be addressed.

Contents

1. Introduction

Single-walled carbon nanotubes (SWCNTs) have a rich variety of physical properties depending on very small differences in how each individual graphene layer is rolled up into a tube. The wide variety of electronic structures in combination with a mechanically strong nanoscale lattice and an exceptionally high thermal conductivity are among the main reasons for the large interest in using SWCNTs in future electronic and optical applications [1]. Unfortunately, scaled-up production of SWCNTs with a specific set of (n,m) indices is still very challenging, necessitating a lot of enrichment after SWCNTs have been synthesized [2]. The promise for new electronic and optical applications of SWCNTs is partly held up by this challenge [1]. There is thus a great need for new characterization methods that are fast, precise and cost-effective to verify the composition of SWCNTs, subsequently enabling the fabrication of devices based on the properties of individual SWCNTs.

Optical spectroscopy can, in spite of its limitations in spatial resolution, provide valuable information about nano-objects [3], including individual SWCNTs [4, 5]. Single-photon excitation processes, such as Raman spectroscopy [6–8], electronic absorption [9], Rayleigh scattering [10] and luminescence [7, 11, 12] have provided information on electronic and phononic structure and their dynamics in SWCNTs. Nonlinear optical techniques, on the other hand, probe the response of the system to multiple interactions with the electromagnetic field, and can therefore provide complementary information. Nonlinear techniques are especially interesting, because nanomaterials can have remarkably large nonlinear optical responses [3]. It can even be anticipated that nonlinear spectroscopy on the single particle level will become an important characterization technique. This would be very desirable for nanomaterials, which are often structurally inhomogeneous. Indeed, four-wave mixing (FWM) in the picosecond regime has been used to image carbon nanotubes (CNTs) on a surface [13] and in the femtosecond regime to address suspended, individual SWCNTs [14]. As a third-order nonlinear process, FWM has no symmetry requirements for the system under study, thus providing a very general capability.

In contrast, second-order processes, such as second-harmonic generation (SHG), are very sensitive to symmetry, and are forbidden in centrosymmetric materials within the electric-dipole approximation of the light–matter interaction [15]. Chirality is a structural property that necessarily breaks centrosymmetry, allowing second-order processes [16]. A vast majority

of SWCNTs are chiral, and SHG has been proposed as a probe of their chirality [17–20]. Beyond chirality itself, the handedness of SWCNTs is important for applications such as molecular recognition [21, 22]. Although Raman spectroscopy has been developed towards the determination of the chiral indices of SWCNTs [8], it is not able to determine the absolute handedness.

SHG has been observed from thin films of SWCNTs [18, 19, 23], and from an ensemble of SWCNTs trapped in zeolites [24]. The latter result was associated with chirality, and a large second-order susceptibility on the order of 400 pm V^{-1}, predicted theoretically [17, 25], was experimentally confirmed. It is, however, not evident *a priori* whether individual SWCNTs have a sufficient second-order response to be detected by SHG. Such SHG from an individual SWCNT could also be interpreted as the most elementary form of hyper-Rayleigh scattering, the term usually used for SHG scattering from an incoherent ensemble of molecules [26].

In this paper, we demonstrate that not only can individual SWCNTs be observed by SHG, but also SHG imaging is possible. Our CNTs are suspended across a slit-opening in a membrane, hence providing a highly symmetric environment for the tubes. Prior to SHG measurements, the CNTs are carefully characterized by transmission electron microscopy (TEM) and electron diffraction (ED) in order to confirm their individuality and determine their chiral indices (*n,m*). In spite of having an individual SWCNT with relatively low chiral angle, its SHG image is observed. The results demonstrate the potential of SHG as a non-destructive tool to study individual SWCNTs and their symmetry properties.

2. Experiment

2.1. Sample preparation

Our samples consist of SWCNTs grown with chemical vapor deposition (CVD) across a 1.2 μm wide slit opening in a 300 nm thick Si_3N_4 membrane. A schematic of the sample geometry is shown in figure 1. The sample preparation starts from a 500 μm thick, double side polished ⟨100⟩ Si wafer with a 300 nm thick dielectric layer of Si_3N_4 on both sides. First, a 750 μm × 750 μm opening in the bottom Si_3N_4 layer was made, using optical lithography followed by reactive ion etching (RIE) at a pressure of 55 mTorr and 150 W power with a gas flow of 50 sccm of CHF_3 and 5 sccm of O_2. This was followed by wet etching through the Si wafer in 35% KOH at 97 °C, with an etch rate of 180 μm h^{-1}. The etching process is anisotropic with an etching angle of 54.7°, resulting in a 50 μm × 50 μm Si_3N_4 membrane window on the front side. A slit opening with the dimensions 1.2 μm × 40 μm was then made in the Si_3N_4 membrane, using electron beam lithography followed by a second RIE step. The bottom of the sample was then covered by a 25 nm thick layer of tantalum, chosen for its high melting point, which enables it to survive during the CVD of CNTs. The metal layer supports the membrane and can be used for gating purposes. SWCNTs were grown across the membrane in a vertical CVD reactor. CO was used as the carbon source, Ni as the catalyst material and the CNT growth temperature was 750 °C. The SWCNT synthesis is described in more detail elsewhere [27, 28].

2.2. Transmission electron microscopy and electron diffraction characterization

The morphology and structure of the suspended CNTs were characterized prior to SHG imaging in a Philips CM200-FEG TEM, which is equipped with a Gatan 794 multiscan charge-coupled

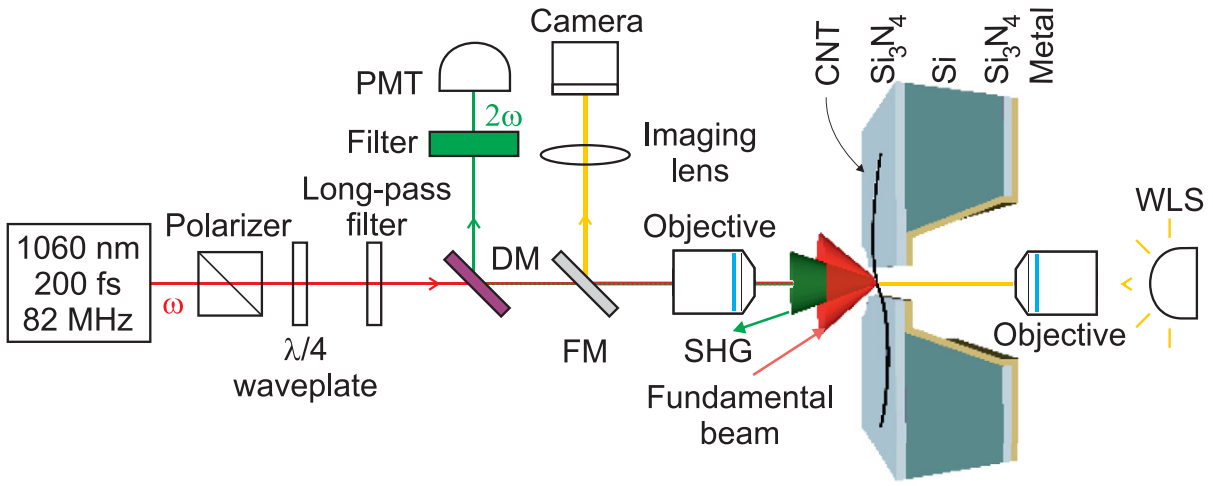

Figure 1. Schematics of sample geometry and SHG microscopy setup. The SWCNTs are suspended across a 1.2 μm wide slit opening in a 300 nm thick Si_3N_4 membrane. A pulsed and collimated beam from an ultrafast laser was passed through a polarizer and a quarter-wave plate to generate circularly polarized light and focused to the sample by an objective (NA = 0.8). A long-pass filter was used after the polarization optics to block SHG from those elements. Reflected SHG (2ω) was separated from the fundamental excitation wavelength (ω) by a dichroic mirror (DM) and an interference filter and detected by a photomultiplier tube (PMT). A white-light source (WLS), camera and flip mirror (FM) were used to find the sample before SHG imaging.

device camera for digital data recording. Both direct imaging and ED patterning were used in several locations along the nanotube bridges to study their composition and chiral properties. To minimize the risk of electron beam induced damage to the CNT lattice, a low acceleration voltage of 80 kV and short exposure times of 3 s were used. Thus the electrons in the beam carried significantly lower energy than the threshold of about 100 keV for knock-on damage to remove a carbon atom from the CNT lattice [29, 30].

For the sample in figure 2(a), CNTs were found at two locations, creating nanometer-wide bridges across the slit opening. ED patterning revealed that the nano-bridge on the left consists of a bundle of 4–5 CNTs. The nano-bridge on the right was confirmed to be an individual SWCNT, except at the almost horizontal section close to the upper edge, where at least one other short CNT is bundled to it. The ED pattern from the individual SWCNT is shown in figure 2(b), from which the chiral indices of the SWCNT were determined to be (42,1), using intrinsic layer-line distance analysis [31]. The chiral indices denote the number of lattice base vectors needed to describe the roll-up vector, and thereby define the lattice structure of the SWCNT. In the present case the nanotube has a diameter of 3.3 nm and a chiral angle (i.e. the smallest angle between the tube cross-section and a lattice base vector) of 1.2°. The appearance of separated layer-lines in the ED pattern (arrows in figure 2(b)) confirms that the SWCNT is chiral [32]. The TEM image shown in figure 2(a) was taken in a JEOL JEM-2200FS microscope after the SHG measurement.

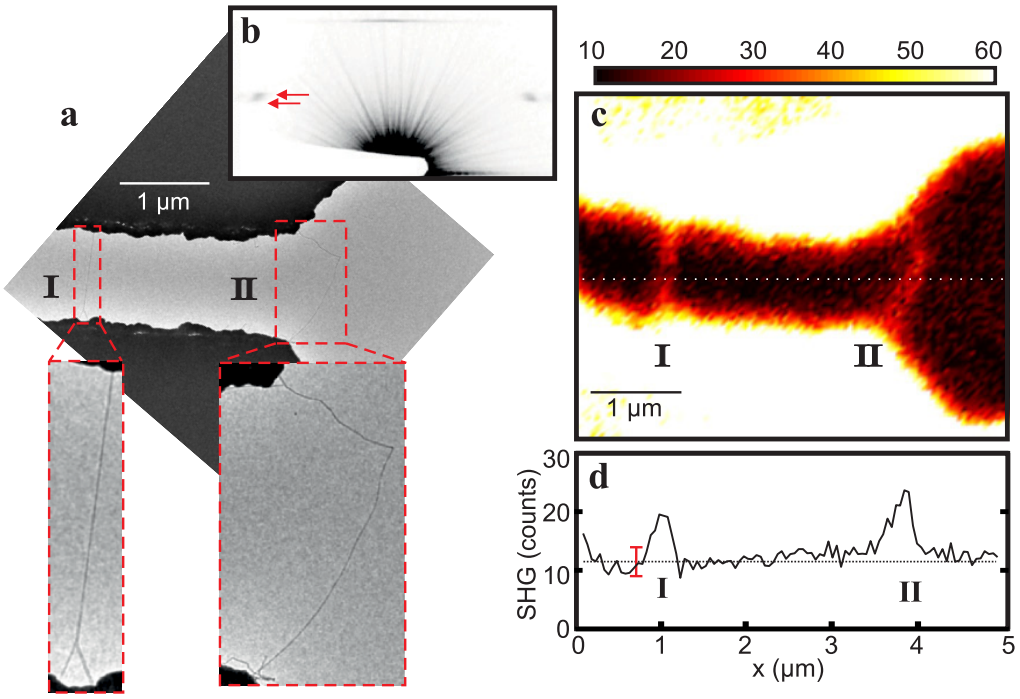

Figure 2. TEM and SHG characterization of suspended SWCNTs. (a) TEM image of the sample, featuring a bundle of 4–5 CNTs on the left (I) and an individual SWCNT on the right (II) suspended across the horizontal slit opening (bright area) in the Si_3N_4 membrane (dark area). (b) ED pattern from (II). The separated layer-lines indicated by two arrows clearly demonstrate that the nanotube has a chiral structure, which is very close to a zigzag tube. (c) SHG image of the sample showing the two suspended SWCNT structures (I and II) over the air slit. (d) A line profile, formed by averaging eight adjacent line profiles, was taken from the SHG image (dotted white line in (c)) to visualize the SNR of the measurement. The mean background value (11.5 counts) of the measurement is shown as a dotted line and the calculated standard deviation (5 counts) as a red bar.

2.3. Second-harmonic generation (SHG) microscopy

The SHG microscope setup is schematically shown in figure 1. The light source was a mode-locked Nd:glass laser emitting an 82 MHz train of 200 fs pulses centered at the wavelength of 1060 nm. The average power of the pulsed laser beam was around 1 mW to avoid sample damage. The input beam was expanded to a diameter of 7 mm, spatially filtered, well collimated and polarized before entering the focusing objective (NA = 0.8). The diameter of the focused laser spot was about 800 nm.

The structure and non-vanishing components of the second-order susceptibility tensor depend on material symmetry, giving rise to polarization-dependent SHG response. In order to facilitate coupling of the fundamental laser beam with all the possible components of the tensor and for any orientation of the SWCNTs, a calcite Glan polarizer was used to clean up the linear polarization of the beam and a subsequent quarter-wave plate was used to change the

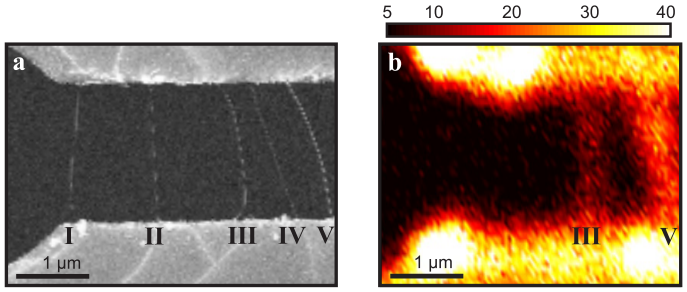

Figure 3. (a) SEM and (b) SHG images of SWCNTs suspended across the horizontal slit opening (dark area) in the Si_3N_4 membrane (bright area). The Roman numerals mark the position of SWCNT nano-bridges. Interestingly, only some of the nano-bridges are visible in the SHG image.

polarization to circular. SHG detection on the other hand was unpolarized to collect as much light as possible with no accidental discrimination.

The SHG light was collected by the same objective and separated from the fundamental and possible two-photon fluorescent light by consecutive long-pass dichroic mirror and narrowband interference filter (16.5 nm bandwidth centered at 532 nm), and detected by a cooled photomultiplier tube connected to a photon counting unit. To ease the sample positioning, a white-light imaging arm was implemented in the microscope. To avoid changes to the input polarization of the laser beam due to the imaging arm, a flip mirror was used to steer the white light to the imaging lens and a consecutive camera when needed.

Imaging was done by raster scanning the sample at the focal plane of the microscope objective using a three-axis piezo-actuated translation stage. All SHG images were acquired within a 5 μm $\times$ 5 μm scanning area using a pixel dwell time of 150 ms, and averaged twice.

3. Results

The SHG image is shown in figure 2(c), clearly depicting the SWCNTs suspended over the slit. Note that the strong background signal from Si_3N_4 prevented SHG visualization of SWCNTs on top of the membrane. The signal-to-noise ratio (SNR) for the suspended part of the SWCNT was estimated from a line profile, formed by averaging eight adjacent line profiles to be ~ 2 (shown in figure 2(d), with its location as a dotted line in figure 2(c)). While the SNR is small, the features are distinct and correspond well to the TEM image.

In order to verify that the data is not coincidental and specific to this sample only, we performed measurements on additional samples and observed similar data from eight different CNTs. Although the individuality and chiral indices of these additional CNTs were not determined (most of them are probably bundles), the SHG signals always correlated well with the TEM or scanning electron microscope (SEM) images. Figure 3 shows SEM and SHG images taken from a sample with several nanotube bridges, marked by Roman numerals I–V. Interestingly, not all the nanotube bridges show up in the SHG image. This could imply that resonance enhancement plays an important role in SHG from the nanotubes. Another possible explanation is that the dark tubes are achiral and thus not SHG-active. In addition, we observed that for some of the nanotubes the SHG signal degrades with time with no sign of recovery.

The reason for signal degradation from some of the nanotubes is not clear, as the CNTs after SHG measurements are confirmed still present by TEM or SEM imaging.

The SHG signal vanishes rapidly below the noise level as the excitation power is reduced, and it is difficult to reliably measure its spectrum or verify its quadratic dependence on the fundamental intensity. Furthermore, the quadratic dependence is characteristic to any two-photon-excited process and, as such, does not provide distinctive evidence of the SHG origin of the signal. We therefore provide estimates for the SHG signal response, as well as for other possible origins of the signal to carefully exclude them.

We first estimate the expected SHG signal strength by assuming that the second-order susceptibility of CNTs is equal to 400 pm V^{-1}, as reported from measurements on an ensemble of SWCNTs trapped in zeolites [24]. (See appendix for calculation details.) This value is more than a factor of 100 larger than the typical scale of second-order susceptibility for conventional materials, but still about ten times smaller than what has been predicted by two independent theoretical studies [17, 25]. In consequence, our modest 1 mW average laser power and 8.0×10^{-7} m focused spot size, should give rise to a very large SHG source polarization of 1.6×10^{-4} W s V^{-1} m^{-2}, yielding a source dipole moment of 9.1×10^{-28} W m s V^{-1} within the illuminated volume. By neglecting field polarization effects, this dipole moment emits a total power of 8.7×10^{-8} W into all solid angles. Averaged over time this gives 1.4×10^{-12} W for continuous emitted power. The combined light collection efficiencies of the objective ($\sim 10^{-1}$), dichroic and interference filters ($\sim 10^{-1}$) and detector ($\sim 10^{-1}$), yields an estimated SHG signal count rate of 3.8×10^{3} s^{-1}. This is about 50 times higher than the measured signal of 77 counts s^{-1}. Note, however, that the maximum second-order susceptibility is found at excitation energies resonant with the electronic level structure of the CNT [24, 25], and the measured signal scales quadratically with susceptibility. The difference between our experiment and the estimate could therefore be due to measuring off resonance, rendering the effective susceptibility to be about 57 pm V^{-1} for our particular tube. Indeed, Pedersen and Pedersen [25] predict the resonances to shift to lower energies as the CNT diameter increases, with CNTs of similar diameter having their strongest resonances well below our fundamental excitation energy of 1.17 eV.

We support this observation by calculating the electronic level structure of our (42,1) CNT. Using an empirical relation between the tube structure and electronic resonance energies [11], we estimate that E_{11} for our (42,1) tube is 0.34 eV. Sfeir *et al* [33] have measured several excitonic transitions for thick tubes and obtained transition energy relations for $E_{ii}/E_{11} (i = 2, 3, 4)$. Using their relations for the (42,1) tube gives 0.60, 1.19 and 1.45 eV for E_{22}, E_{33} and E_{44}, respectively. Another empirical relation based on a large set of Rayleigh scattering measurements gives for the same transitions similar estimates, 0.56, 1.14 and 1.50 eV, respectively [34]. From these, E_{33} is close to our fundamental excitation energy of 1.17 eV (wavelength 1060 nm), suggesting that one-photon resonance is possible. Note, however, that the strongest signal enhancements are predicted for E_{11} and E_{22}, and the E_{33} resonance is expected to be considerably weaker [25]. For the second-harmonic excitation at 2.34 eV, only the latter empirical formula is able to give an estimate of nearby transitions [34], returning E_{77} with an energy of 2.40 eV as the closest transition. On the other hand, we did not observe any visible Raman signal from our SWCNTs when using an input wavelength of 532 nm, suggesting that there is no two-photon resonance in our case.

To summarize these observations, we would like to point out that the estimates based on literature values from experiments and theory [17, 25] surprisingly suggest that SHG imaging

may be relatively straightforward for small diameter semiconducting SWCNTs of higher chiral angle, where two-photon resonances could be accessed by available laser systems. Our present results are in full agreement with this.

We will now proceed to exclude other optical processes by estimating an upper boundary to their contribution. First we consider scattering of fundamental light into our detector as a source of the signal. We assume that the linear susceptibility of the CNT is on the order of unity [35]. By a similar calculation, we obtain a source dipole moment of $7.6 \times 10^{-27}\,\mathrm{W\,m\,s\,V^{-1}}$ and a signal count rate of $3.3 \times 10^{7}\mathrm{counts\,s^{-1}}$, which is in good agreement with [35]. However, our setup has a strong discrimination between the fundamental and SHG wavelengths from the dichroic mirror (>10), from the interference filter ($>10^5$), and from the detector efficiency ($>10^3$). The discrimination is therefore at least nine orders of magnitude, and most likely much higher. The scattered signal is thus at most $3.3 \times 10^{-2}\,\mathrm{s^{-1}}$, which is three orders of magnitude smaller than the detected signal. To verify this we replaced the SWCNT sample with a strong scatterer (mirror). The signal then vanished completely, and did not reappear even after 20-fold increase in the input laser power. This observation is consistent with the data in figure 3(b), where some CNTs are not visible, thereby excluding scattering of fundamental light (or SHG from preceding components) as the origin of the signal.

We next consider linear and multiphoton absorption induced luminescence. It is generally known that irrespective of the excitation wavelength, luminescence occurs essentially from the lowest bright excitonic state corresponding to the E_{11} emission [12, 36]. This is due to ultrafast non-radiative intraband relaxation of electrons and holes which occurs fully within 100 fs [37]. In fact, as far as we know, there are no reports of photoluminescence of individual SWCNTs above the lowest excitonic emission. Since our experiment is designed to strongly discriminate against emission outside the SHG spectral window we find it very unlikely that fluorescence could be the source of the detected signal. Note that only very narrow CNTs with a diameter less than 0.85 nm have E_{11} emission close to the energy of the fundamental beam (1.17 eV), for which we above found a discrimination of at least nine orders of magnitude. E_{11} emission from our identified (42,1) CNT occurs at an even lower energy, in the mid-IR region (~ 0.34 eV), where our detector is not responsive.

In addition, fluorescence is highly sensitive to any process that affects relaxation. Bundling in particular leads to very efficient quenching of fluorescence due to non-radiative energy transfer and relaxation provided by metallic tubes in bundles. Indeed, originally fluorescence was observed from SWCNTs only after developing a method for debundling SWCNTs [12]. On the contrary, SHG is a coherent process which is not sensitive to energy relaxation phenomena. As we have observed, signal from bundles as well as from at least one individual SWCNT with comparable intensities it is highly unlikely that the signal originates from fluorescence. Moreover, fluorescence has been observed to saturate at fairly low excitation levels of ~ 1 exciton $\mu\mathrm{m}^{-1}$ for suspended SWCNTs [38]. Interestingly, this means that nonlinear signals start to dominate at relatively low excitation intensities.

Within the electric-dipole approximation, there are four possible sources of the SHG signal: chirality, lattice defects, tube deformations and surface interactions. We discard the latter two, since the signal intensity is quite similar and homogeneous and is not visibly affected by tube bending either. Thus, we are left with chirality or defects (or both) as the source of SHG. The observation of a distinct ED pattern establishes that the tube is chiral and indicates a high long-range order, i.e. low defect concentration, making therefore chirality the most plausible source.

The likely chiral origin of the SHG signal provides exciting opportunities for future development. It is possible to enrich a given SWCNT handedness, e.g. by molecular recognition in combination with ultracentrifugation [21, 22]. So far, the only way to confirm the handedness of a specific individual CNT is by scanning probe microscopy [39, 40], or by high-resolution TEM imaging [41–43]. Both methods require vacuum environment, and are time consuming and potentially damaging to the CNT. SHG microscopy might offer a much faster and non-destructive technique, and its sensitivity to chirality has been well-established [44–50]. In addition, since SHG is forbidden from centrosymmetric materials, SHG microscopy might provide capabilities to characterize SWCNTs on substrates, provided that the used substrate would be centrosymmetric (e.g. isotropic glass).

In order to develop SHG microscopy as a probe of absolute handedness for SWCNTs, additional work is needed. The components of the second-order susceptibility can be classified as achiral or chiral. The former are non-vanishing for any non-centrosymmetric system, whereas the latter rely on chirality. In addition, the chiral components reverse their sign between the two handednesses of the chiral sample. The chiral signatures in SHG responses arise from a complex interplay between achiral and chiral susceptibility components leading to different SHG signals [51–53] depending on the handedness of the sample. The defect-free SWCNTs possess only chiral components, which will only lead to changes in the phase of the SHG signal depending on the handedness. Thus polarization-based SHG techniques as such should not provide information of the absolute handedness of SWCNTs but phase sensitive SHG techniques should be used [54, 55]. For example, if the SWCNT is lying on a carefully selected surface, such that it provides an achiral mixing signal that will interfere with the chiral signal from the SWCNT, it may result in a detectable difference in the signal depending on the handedness of the excitation light.

It is also crucial to increase the SNR for spectral analysis and handedness measurements. Higher excitation power and shorter pulses would increase the SNR, but are limited by sample damage. Another possibility would be to perform measurements closer to resonant conditions, either by tuning the excitation wavelength or by measuring different types of SWCNTs. But while the mechanism for sample damage remains unclear, the best approach for SNR improvement is not clear since resonant excitation conditions might also increase sample damage. Thus for proof-of-principle handedness measurements, single point SHG detection, instead of imaging, could be performed and the SNR could be improved by increasing the measurement time from the present 150 ms per pixel.

SHG can also occur in centrosymmetric materials when interactions beyond electric dipoles (magnetic and quadrupole interactions) are taken into account. Such higher-multipole effects are expected to be significantly weaker than electric-dipole effects [56], but would allow SHG from achiral SWCNTs. To fully justify SHG as a probe of chirality of SWCNTs it will be important to study the origin of SHG from individual SWCNTs in more detail.

While we conclude that defects are not likely to explain our observations, SHG does have additional opportunities in imaging of defects. An ideal SWCNT has very high symmetry, and defects will decrease the overall symmetry and introduce new non-vanishing susceptibility components, which change the characteristics of the local SHG response. Due to its sensitivity to symmetry breaking, SHG could therefore provide a complementary technique for non-destructive and label-free visualization of defects in SWCNTs.

4. Summary

To conclude, we have observed SHG from an individual, air-suspended SWCNT. Although the SNR of the present results remains low, careful analysis of the experimental conditions excludes all other possible mechanisms, leaving SHG as the most likely explanation of the results. The SHG signal most likely originates from the breaking of centrosymmetry of the SWCNT by its non-zero chiral angle. We propose that SHG could be used to measure the handedness of SWCNTs and visualize defects in SWCNTs, providing a valuable tool for the study and characterization of SWCNTs. In order to fulfill this potential, several issues need to be addressed to obtain a better understanding of the dependence of SHG on the structural features of the SWCNTs. Finally, SHG techniques are fully compatible with existing nonlinear optical techniques, such as FWM, and could in the future easily be implemented for multimodal measurements of nanomolecules.

Acknowledgments

This study was supported by the Academy of Finland (project numbers 122620, 128445, 134973, 135062 and 7122008) and CNB-E project of Aalto University MIDE program for funding. In addition, MJH acknowledges support from Modern School of Optics and Photonics in Finland, AJ and MJH from Emil Aaltonen foundation and OH from Jenny and Antti Wihuri foundation.

Appendix. Calculation of the SHG count rate from an individual SWCNT

To predict the strength of the SHG signal emitted by the SWCNT, we start by calculating the magnitude of the second-order source polarization in the form [57]

$$P_{2\omega} = 2\varepsilon_0 \chi^{(2)} E_\omega^2, \tag{A.1}$$

where ε_0 is the permittivity of free space, $\chi^{(2)}$ is the second-order nonlinear optical susceptibility and E_ω is the electric field strength at the fundamental frequency ω. In addition, the intensity of the fundamental field is

$$I_\omega = 2\varepsilon_0 c E_\omega^2, \tag{A.2}$$

where c is the speed of light in vacuum.

Combining equations (A.1) and (A.2) yields the second-order source polarization during the peak of the excitation pulse

$$P_{2\omega} = \frac{\chi^{(2)} I_\omega}{c}. \tag{A.3}$$

Note that in our experiment, we used a pulsed laser with a wavelength λ_ω of 1.06×10^{-6} m, pulse width τ of 2.0×10^{-13} s, and repetition rate R of 8.2×10^7 Hz. Thus, the duty cycle of our laser

$$d = \tau R \tag{A.4}$$

corresponds to a value equal to 1.6×10^{-5}.

Using a focusing objective with a numerical aperture (NA) of 0.8, the resulting diameter s of the focused laser beam

$$s = 0.61\frac{\lambda_\omega}{NA} \tag{A.5}$$

is about 8.0×10^{-7} m.

With an average input power $\langle P_\omega \rangle$ of 1×10^{-3} W, we obtain the peak intensity at the focus

$$I_\omega = 4\frac{\langle P_\omega \rangle}{\pi s^2 d} \tag{A.6}$$

which is equal to 1.2×10^{14} W m^{-2}.

Combining our peak intensity estimate and the second-order susceptibility value of CNTs, which is assumed to be 4.0×10^{-10} m V^{-1} as reported in [24], we therefore obtain from equation (A.3) a SHG source polarization of 1.6×10^{-4} W s V^{-1} m^{-2}.

The effective volume V for the source polarization is limited in the two transverse directions by the CNT diameter (3.0×10^{-9} m) and in the longitudinal direction by the diameter of the focused laser beam (8.0×10^{-7} m), yielding a volume of 5.7×10^{-24} m^3.

Thus, the magnitude of the source dipole moment $p_{2\omega}$ can be directly calculated as

$$p_{2\omega} = P_{2\omega} V. \tag{A.7}$$

This results in a source dipole moment of 9.1×10^{-28} W m s V^{-1} within the illuminated volume.

By assuming that the effective dipole at the second-harmonic frequency acts as a point source and by neglecting any polarization effects, the second-harmonic field $E_{2\omega}$ at distance r is

$$E_{2\omega} = \frac{p_{2\omega} k_{2\omega}^2}{4\pi\varepsilon_0 r}, \tag{A.8}$$

where $k_{2\omega}$ is the wave vector at the second-harmonic frequency, $k_{2\omega} = \frac{2\pi}{\lambda_{2\omega}}$.

This field strength corresponds to the second-harmonic intensity

$$I_{2\omega} = 2\varepsilon_0 c E_{2\omega}^2 = \frac{2c p_{2\omega}^2 k_{2\omega}^4}{(4\pi\varepsilon_0)(4\pi r^2)}. \tag{A.9}$$

For our simple estimate, where polarization effects are not considered, this intensity is radiated symmetrically to all directions. The total second-harmonic power emitted to all directions is thus

$$P_{2\omega} = I_{2\omega}(4\pi r^2). \tag{A.10}$$

By combining equations (A.7)–(A.10), we obtain the total second-harmonic power emitted to all directions during the peak of the excitation pulse that is equal to 8.7×10^{-8} W.

Using the duty cycle of our laser, we can therefore estimate the time-averaged second-harmonic power

$$\langle P_{2\omega} \rangle = P_{2\omega}\, d \tag{A.11}$$

which is equal to 1.4×10^{-12} W.

In addition, the energy of the second-harmonic photons is

$$W_{2\omega} = \frac{hc}{\lambda_{2\omega}}, \tag{A.12}$$

where h is the Planck constant, yielding a photon energy of 3.8×10^{-19} J.

Using equations (A.11) and (A.12), we finally obtain the SHG signal count rate

$$N_{2\omega} = \frac{\langle P_{2\omega} \rangle}{W_{2\omega}} \tag{A.13}$$

which is equal to $3.8 \times 10^{6}\ \mathrm{s}^{-1}$.

Finally, we need to account for the light collection efficiency of our detection system. The NA of the objective collects only 10% of the light emitted in all directions, the dichroic and interference filters transmit about 10% of light and the detector efficiency is 10%. The final estimate for the signal count rate is thus $3.8 \times 10^{3}\ \mathrm{s}^{-1}$.

References

[1] Avouris P, Chen Z and Perebeinos V 2007 Carbon-based electronics *Nature Nanotechnol.* **2** 605–15

[2] Hersam M C 2008 Progress towards monodisperse single-walled carbon nanotubes *Nature Nanotechnol.* **3** 387–94

[3] Wang Y, Lin C Y, Nikolaenko A, Raghunathan V and Potma E O 2011 Four-wave mixing microscopy of nanostructures *Adv. Opt. Photon.* **3** 1–52

[4] Hartschuh A, Pedrosa H N, Peterson J, Huang L, Anger P, Qian H, Meixner A J, Steiner M, Novotny L and Krauss T D 2005 Single carbon nanotube optical spectroscopy *Chem. Phys. Chem.* **6** 567–74

[5] Sfeir M Y *et al* 2006 Optical spectroscopy of individual single-walled carbon nanotubes of defined chiral structure *Science* **312** 554

[6] Hartschuh A, Sánchez E J, Xie X S and Novotny L 2003 High-resolution near-field Raman microscopy of single-walled carbon nanotubes *Phys. Rev. Lett.* **90** 095503

[7] Hartschuh A, Pedrosa H N, Novotny L and Krauss T D 2003 Simultaneous fluorescence and Raman scattering from single carbon nanotubes *Science* **301** 1354–6

[8] Michel T, Paillet M, Nakabayashi D, Picher M, Jourdain V, Meyer J C, Zahab A A and Sauvajol J L 2009 Indexing of individual single-walled carbon nanotubes from Raman spectroscopy *Phys. Rev.* B **80** 245416

[9] Bachilo S M, Strano M S, Kittrell C, Hauge R H, Smalley R E and Weisman R B 2002 Structure-assigned optical spectra of single-walled carbon nanotubes *Science* **298** 2361–6

[10] Sfeir M Y, Wang F, Huang L, Chuang C-C, Hone J, O'brien S P, Heinz T F and Brus L E 2004 Probing electronic transitions in individual carbon nanotubes by Rayleigh scattering *Science* **306** 1540–3

[11] Weisman R B and Bachilo S M 2003 Dependence of optical transition energies on structure for single-walled carbon nanotubes in aqueous suspension: an empirical Kataura plot *Nano Lett.* **3** 1235–8

[12] O'Connell M J *et al* 2002 Band gap fluorescence from individual single-walled carbon nanotubes *Science* **297** 593–6

[13] Kim H, Sheps T, Collins P G and Potma E O 2009 Nonlinear optical imaging of individual carbon nanotubes with four-wave-mixing microscopy *Nano Lett.* **9** 2991–5

[14] Myllyperkiö P *et al* 2010 Femtosecond four-wave-mixing spectroscopy of suspended individual semiconducting single-walled carbon nanotubes *ACS Nano* **4** 6780–6

[15] Shen Y R 1989 Surface properties probed by second-harmonic and sum-frequency generation *Nature* **337** 519–25

[16] Petralli-Mallow T, Wong T M, Byers J D, Yee H I and Hicks J M 1993 Circular dichroism spectroscopy at interfaces: a surface second harmonic generation study *J. Phys. Chem.* **97** 1383–88

[17] Guo G Y, Chu K C, Wang D and Duan C 2004 Linear and nonlinear optical properties of carbon nanotubes from first-principles calculations *Phys. Rev.* B **69** 205416
[18] De Dominicis L, Fantoni R, Botti S, Ciardi R, Asilyan L, Fiori A and Orlanducci S 2005 Analysis of the chiral composition of a carbon nanotube surface by means of second harmonic generation *J. Raman Spectrosc.* **36** 165–70
[19] Akimov D A *et al* 2004 Second- and third-harmonic generation by carbon nanotubes irradiated with femtosecond laser pulses *J. Exp. Theor. Phys.* **98** 220–6
[20] Konorov S O *et al* 2003 Femtosecond optical harmonic generation as a non-linear spectroscopic probe for carbon nanotubes *J. Raman Spectrosc.* **34** 1018–24
[21] Peng X, Komatsu N, Bhattacharya S, Shimawaki T, Aonuma S, Kimura T and Osuka A 2007 Optically active single-walled carbon nanotubes *Nature Nanotechnol.* **2** 361–5
[22] Tu X, Manohar S, Jagota A and Zheng M 2009 DNA sequence motifs for structure-specific recognition and separation of carbon nanotubes *Nature* **460** 250–3
[23] De Dominicis L, Botti S, Asilyan L S, Ciardi R, Fantoni R, Terranova M L, Fiori A, Orlanducci S and Appolloni R 2004 Second- and third-harmonic generation in single-walled carbon nanotubes at nanosecond time scale *Appl. Phys. Lett.* **85** 1418–20
[24] Su H, Ye J, Tang Z and Wong K 2008 Resonant second-harmonic generation in monosized and aligned single-walled carbon nanotubes *Phys. Rev.* B **77** 125428
[25] Pedersen T and Pedersen K 2009 Systematic tight-binding study of optical second-harmonic generation in carbon nanotubes *Phys. Rev.* B **79** 035422
[26] Clays K and Persoons A 1991 Hyper-Rayleigh scattering in solution *Phys. Rev. Lett.* **66** 2980–3
[27] Mudimela P R, Nasibulin A G, Jiang H, Susi T, Chassaing D and Kauppinen E I 2009 Incremental variation in the number of carbon nanotube walls with growth temperature *J. Phys. Chem.* C **113** 2212–8
[28] Queipo P, Nasibulin A G, Gonzalez D, Tapper U, Jiang H, Tsuneta T, Grigoras K, Duenas J A and Kauppinen E I 2006 Novel catalyst particle production method for CVD growth of single- and double-walled carbon nanotubes *Carbon* **44** 1604–8
[29] Banhart F 1999 Irradiation effects in carbon nanostructures *Rep. Prog. Phys.* **62** 1181
[30] Krasheninnikov A V and Banhart F 2007 Engineering of nanostructured carbon materials with electron or ion beams *Nature Mater.* **6** 723–33
[31] Jiang H, Nasibulin A G, Brown D P and Kauppinen E I 2007 Unambiguous atomic structural determination of single-walled carbon nanotubes by electron diffraction *Carbon* **45** 662–7
[32] Jiang H, Brown D P, Nikolaev P, Nasibulin A G and Kauppinen E I 2008 Determination of helicities in unidirectional assemblies of graphitic or graphiticlike tubular structures *Appl. Phys. Lett.* **93** 141903
[33] Sfeir M Y, Misewich J A, Rosenblatt S, Wu Y, Voisin C, Yan H, Berciaud S, Heinz T F, Chandra B and Caldwell R 2010 Infrared spectra of individual semiconducting single-walled carbon nanotubes: testing the scaling of transition energies for large diameter nanotubes *Phys. Rev.* B **82** 195424
[34] Liu K *et al* 2011 An atlas of carbon nanotube optical transitions *Nature Nanotechnol.* **7** 325–9
[35] Heinz T F 2007 *Rayleigh Scattering Spectroscopy Carbon Nanotubes: Advanced Topics in the Synthesis, Structure, Properties and Applications* ed A Jorio, M S Dresselhaus and G Dresselhaus (Berlin: Springer) chapter 11 pp 353–68
[36] Lefebvre J, Homma Y and Finnie P 2003 Bright band gap photoluminescence from unprocessed single-walled carbon nanotubes *Phys. Rev. Lett.* **90** 217401
[37] Ma Y-Z, Stenger J, Zimmermann J, Bachilo S M, Smalley R E, Weisman R B and Fleming G R 2004 Ultrafast carrier dynamics in single-walled carbon nanotubes probed by femtosecond spectroscopy. *J. Chem. Phys.* **120** 3368–73
[38] Xiao Y F, Nhan T Q, Wilson M and Fraser J M 2010 Saturation of the photoluminescence at few-exciton levels in a single-walled carbon nanotube under ultrafast excitation *Phys. Rev. Lett.* **104** 17401
[39] Wildöer J W G, Venema L C, Rinzler A G, Smalley R E and Dekker C 1998 Electronic structure of atomically resolved carbon nanotubes *Nature* **391** 59–62

[40] Odom T, Huang J, Kim P and Lieber C 1998 Atomic structure and electronic properties of single-walled carbon nanotubes *Nature* **391** 62–4
[41] Liu Z, Suenaga K, Yoshida H, Sugai T, Shinohara H and Iijima S 2005 Determination of optical isomers for left-handed or right-handed chiral double-wall carbon nanotubes *Phys. Rev. Lett.* **95** 187406–6
[42] Hashimoto A, Suenaga K, Urita K, Shimada T, Sugai T, Bandow S, Shinohara H and Iijima S 2005 Atomic correlation between adjacent graphene layers in double-wall carbon nanotubes *Phys. Rev. Lett.* **94** 45504
[43] Meyer R, Friedrichs S, Kirkland A I, Sloan J, Hutchison J L and Green M L 2003 A composite method for the determination of the chirality of single walled carbon nanotubes *J. Microsc.* **212** 152–7
[44] Huttunen M, Erkintalo M and Kauranen M 2009 Absolute nonlinear optical probes of surface chirality *J. Opt. A: Pure Appl. Opt.* **11** 034006
[45] Huttunen M J, Virkki M, Erkintalo M, Vuorimaa E, Efimov A, Lemmetyinen H and Kauranen M 2010 Absolute probe of surface chirality based on focused circularly polarized light *J. Phys. Chem. Lett.* **1** 1826–9
[46] Kriech M A and Conboy J C 2005 Imaging chirality with surface second harmonic generation microscopy *J. Am. Chem. Soc.* **127** 2834–5
[47] Valev V K, Silhanek A V, Smisdom N, De Clercq B, Gillijns W, Aktsipetrov O A, Ameloot M, Moshchalkov V V and Verbiest T 2010 Linearly polarized second harmonic generation microscopy reveals chirality *Opt. Express* **18** 8286
[48] Valev V K, Smisdom N, Silhanek A V, De Clercq B, Gillijns W, Ameloot M, Moshchalkov V V and Verbiest T 2009 Plasmonic ratchet wheels: switching circular dichroism by arranging chiral nanostructures *Nano Lett.* **9** 3945–8
[49] Huttunen M J, Bautista G, Decker M, Linden S, Wegener M and Kauranen M 2011 Nonlinear chiral imaging of subwavelength-sized twisted-cross gold nanodimers [Invited] *Opt. Mater. Express* **1** 46
[50] Valev V K, Silhanek A V, Smisdom N, De Clercq B, Gillijns W, Aktsipetrov O A, Ameloot M, Moshchalkov V V and Verbiest T 2011 Linearly polarized second harmonic generation microscopy reveals chirality: erratum *Opt. Express* **19** 9242–4
[51] Maki J J, Kauranen M and Persoons A 1995 Surface second-harmonic generation from chiral materials *Phys. Rev.* B **51** 1425
[52] Maki J J, Verbiest T, Kauranen M, Van Elshocht S and Persoons A 1996 Comparison of linearly and circularly polarized probes of second order optical activity of chiral surfaces *J. Chem. Phys.* **105** 767
[53] Verbiest T, Van Elshocht S, Kauranen M, Hellemans L, Snauwaert J, Nuckolls C, Katz T J and Persoons A 1998 Strong enhancement of nonlinear optical properties through supramolecular chirality *Science* **282** 913–5
[54] Le Xuan L, Brasselet S, Treussart F, Roch J F, Marquier F, Chauvat D, Perruchas S, Tard C and Gacoin T 2006 Balanced homodyne detection of second-harmonic generation from isolated subwavelength emitters *Appl. Phys. Lett.* **89** 121118
[55] Stolle R, Marowsky G, Schwarzberg E and Berkovic G 1996 Phase measurements in nonlinear optics *Appl. Phys.* B **63** 491–8
[56] Wang F X, Rodríguez F J, Albers W M, Ahorinta R, Sipe J E and Kauranen M 2009 Surface and bulk contributions to the second-order nonlinear optical response of a gold film *Phys. Rev.* B **80** 233402
[57] Boyd R W 2008 *Nonlinear Optics* (Amsterdam: Elsevier)